RESEARCH ARTICLE

Key Points:
- We quantify hillslope-scale, near-surface rock strength on a regional scale using the Culmann and Newmark hillslope-stability models
- Strength estimates are generally low, with cohesion model predictions less than 60 kPa for friction angle predictions of 24° to 44°
- The cohesion of young sedimentary rocks in the shallow subsurface increases with increasing maximum burial depth

Supporting Information:
- Supporting Information S1
- Data Set S1
- Table S1
- Table S2
- Table S3

Correspondence to:
K. F. Townsend,
kirkft@umich.edu

Quantifying Near-Surface Rock Strength on a Regional Scale From Hillslope Stability Models

Kirk F. Townsend[1] [ID], Sean F. Gallen[2,3] [ID], and Marin K. Clark[1]

[1]Department of Earth and Environmental Sciences, University of Michigan, Ann Arbor, MI, USA, [2]Department of Earth Sciences, ETH Zürich, Zürich, Switzerland, [3]Now at Department of Geosciences, Colorado State University, Fort Collins, CO, USA

Abstract Rock strength is a fundamental property of earth materials that influences the morphology of landscapes and modulates feedbacks between surface processes, tectonics, and climate. However, rock strength remains challenging to quantify over the broad spatial scales necessary for geomorphic investigations. Consequently, the factors that control rock strength in the near-surface environment (i.e., the critical zone) remain poorly understood. Here we quantify near-surface rock strength on a regional scale by exploiting two hillslope-stability models, which explicitly relate the balance of forces within a hillslope to Mohr-Coulomb strength parameters. We first use the Culmann finite-slope stability model to back-calculate static rock strength with high-density measurements of ridge-to-channel hillslope height and gradient. Second, we invert the Newmark infinite-slope stability model for strength using an earthquake peak ground acceleration model and coseismic landslide inventory. We apply these two model approaches to a recently inverted sedimentary basin in the eastern Topatopa Mountains of southern California, USA, where a tectonic gradient has exposed stratigraphic units with variable burial histories. Results show similar trends in strength with respect to stratigraphic position and have comparable strength estimates to the lowest values of published direct-shear test data. Cohesion estimates are low, with Culmann results ranging from 3 to 60 kPa and Newmark results from 6 to 30 kPa, while friction angle estimates range from 24° to 44° from the Culmann model. We find that maximum burial depth exerts the strongest control on the strength of these young sedimentary rocks, likely through diagenetic changes in porosity, cementation, and ultimately, lithification.

1. Introduction

Rock mass strength has long been recognized as a major control on landscape morphology and evolution (Gilbert, 1877; Hack, 1975). Rock strength governs the ability of material to be dislodged and transported by surface processes and modulates feedbacks between tectonics, climate, and surface processes in mountain belts (Montgomery & Brandon, 2002; Selby, 1980, 1993). Despite this general recognition, many of the factors controlling rock strength are less widely appreciated or quantified. Understanding the interdependences of factors that control rock strength is of broad interest because it is applicable to geotechnical analyses of hillslope stability (Frattini & Crosta, 2013; Hoek & Brown, 1980; Selby, 1980), process models of weathering (Riebe et al., 2017), erosion and sediment transport on hillslopes (Larsen et al., 2010) and in channels (Bursztyn et al., 2015; Sklar & Dietrich, 2001), and overall landscape evolution rates (Forte et al., 2016; Gallen, 2018; Molnar et al., 2007; Roy et al., 2015). Rock strength is also expected to exert a control on the local relief structure of mountain ranges (Montgomery & Brandon, 2002; Schmidt & Montgomery, 1995; Whipple et al., 1999), but untangling the role of rock strength from tectonic and climatic drivers is inhibited by the difficulties in the quantification of this property at the appropriate spatial scale.

Measuring rock strength at spatial scales relevant for geomorphic investigations remains an outstanding challenge due to the scale-dependent nature of strength (Hoek & Brown, 1980, 1997; Schmidt & Montgomery, 1995). "Strength," defined here as the maximum shear stress a material can sustain before failure, is commonly described using Mohr-Coulomb failure criteria (cohesion and angle of internal friction) for properties on the sliding plane of a failure mass. While laboratory tests of rock strength are conducted on intact hand-sized samples, we know that fractures and discontinuities in a rock mass set the upper limit on strength at the hillslope-scale (Gallen et al., 2015; Hoek & Brown, 1980, 1997). Consequently,

laboratory tests can overestimate hillslope-scale strength by an order of magnitude (Schmidt & Montgomery, 1995). The effect and behavior of discontinuities on rock mass strength can be effectively captured at the outcrop-scale using field observations coupled with ranked classification schemes (e.g., GSI and RMC) that penalize intact rock strength by the density, orientation, and surface conditions of fractures (e.g., Hoek & Brown, 1997). However, such classifications require detailed field investigations, and we lack a general, theoretical basis for relating weakening and discontinuity characteristics to rock mass strength that can be applied to a regional scale. Consequently, these approaches are not scalable to entire watersheds or mountain belts, nor are they easily applied to areas that lack observational data.

In this study, we test two approaches to quantifying rock mass strength at regional scales based on slope stability models, digital topography and coseismic landslide inventories. One approach uses static properties of hillslopes extracted from digital elevation models (DEMs) to estimate minimum strength (Culmann, 1875; Schmidt & Montgomery, 1995). This approach may be generally exportable to other settings as a way to quantify rock strength from DEMs. The second approach leverages earthquake-driven landslide inventories as a means to invert for rock strength properties using a dynamic model in which the forces from strong ground motion cause landsliding (Gallen et al., 2015). Because resisting and driving forces are estimated rather than assumed, the latter may be a more robust measure of rock strength but is only applicable where requisite data exist. Using these two techniques in concert allows us to assess the reproducibility of strength values and confidence in our results. The spatial distribution afforded by these methods allows us to quantify rock strength across a tectonic gradient, where differences in fault motion have exposed sedimentary rocks with variable burial and exhumation histories.

2. Field Setting

2.1. Basin Inversion in the Western Transverse Ranges

A setting with a simple tectonic inversion offers several advantages to understanding how rock strength evolves through time. Inversion is marked by a transition from an extensional setting where sediments are deposited and buried in basins to form sedimentary rocks, followed by a subsequent stage where normal faults are reactivated as reverse faults due to crustal shortening. Slip on reverse faults exposes sedimentary rocks deposited in former basins to form incipient mountain ranges. These settings commonly contain stratigraphic sequences that are well dated, and monotonic exhumation histories suggest that these sedimentary rocks lack inherited deformation from previous tectonic events, which can dominate the spatial distribution of rock strength in some regions (i.e., DiBiase et al., 2018; Molnar et al., 2007). This simple history enables us to assess the variability of strength with respect to stratigraphic depth and active upper crustal structures. Furthermore, inversion is a common process in the geological record, so findings here are likely broadly applicable.

The Western Transverse Ranges of southern California, USA, represent an example of an inverted basin (Figure 1). These ranges are composed predominately of late-Cretaceous through Plio-Pleistocene marine and nonmarine clastic sedimentary rocks that were deposited during multiple stages of regional extension and basin formation (Namson & Davis, 1988). Cretaceous through Eocene marine sandstones and shales followed by Oligocene sandstones and conglomerates were deposited in an extensional setting, with specific facies dependent on relative sea level (Atwater, 1998; Prothero & Vance, 1996). The region transitioned to a transtensional tectonic regime as it underwent over 90° of clockwise rotation following complete subduction of the Farallon Plate in early Miocene time (Hornafius et al., 1986; Nicholson et al., 1994). Thick sections of marine siliceous mudstones, sandstones, conglomerates, and volcaniclastic rocks produced by syn-tectonic volcanism accumulated in fault-bounded extensional basins, which continued through Pliocene time (Namson & Davis, 1988; Wright, 1991). Eastward migration of the North American-Pacific plate boundary at 5–6 Ma lead to the development of a transpressional ~160 km "Big Bend" in the San Andreas Fault, which drives the modern regional shortening in the Western Transverse Ranges and caused many normal faults to reactivate as high-angle reverse faults (Dolan et al., 1995; Hornafius et al., 1986; Huftile & Yeats, 1996; Wright, 1991). The late-Mesozoic through Cenozoic sedimentary and volcaniclastic rocks sequences are now being inverted along east-west trending oblique-reverse faults forming the modern mountainous topography.
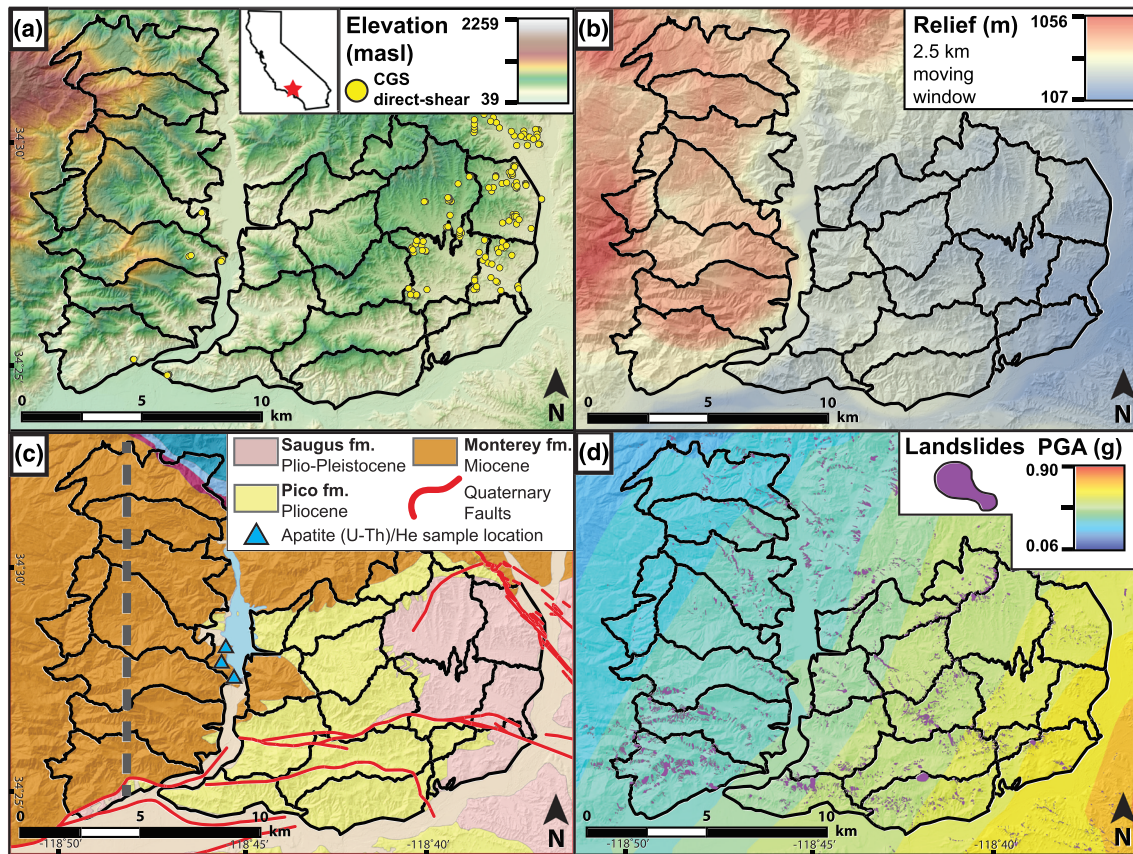
Figure 1. Measurement regions (black polygons) for rock strength estimates from the Culmann and Newmark models in the eastern Topatopa Mountains, southern California. (a) Elevation. Locations sampled for direct-shear tests in the California Geological Survey (CGS) borehole inventory are shown (yellow). Note that samples were typically collected from multiple depth intervals in each borehole and that multiple samples have the same map-view location. See Figure S2 for the complete map of rock samples used to calculate average strength estimates reported in Table 1. (b) Relief calculated within a 2.5-km moving window. (c) Mapped geologic units, which include the Miocene Monterey Formation, the Pliocene Pico Formation, and the Pliocene/Pleistocene Saugus Formation (Dibblee, 1991, 1993, 1996; Dibblee & Ehrenspeck, 1996; U.S. Geological Survey, 2006). Dashed gray line shows location of the geologic cross section in Figure 9. (d) Shakemap PGA raster (Earle et al., 2009; U.S. Geological Survey, 1994) and coseismic landslides produced during the 1994 M_w 6.7 Northridge Earthquake.

2.2. Eastern Topatopa Mountains Study Site

We focus our study on the easternmost Topatopa Mountains, along the northeast margin of the Western Transverse Ranges (Figure 1). Here the mountains expose a section of young (Miocene to Plio-Pleistocene) and variably lithified sedimentary rocks in a broad homocline that dips to the east with strike perpendicular to the range front (Dibblee, 1991, 1993; Dibblee & Ehrenspeck, 1996). Stratigraphic units have similar lithology (primarily clastic rocks) and a simple tectonic history of basin inversion with no inherited deformation, allowing us to assess the variability of strength with respect to stratigraphic depth and active structures. These rocks are being uplifted due to active reverse faulting along the San Cayetano Fault, which initiated during Pliocene time (Dolan & Rockwell, 2001; Huftile & Yeats, 1996; Rockwell, 1988). These stratigraphic units are faulted and folded proximal to the San Cayetano Fault, allowing us to assess how strength varies with stratigraphic depth and exhumation within individual formations. Here a high-resolution (3-m pixel resolution) digital topographic data set has already been produced by the National Oceanographic and Atmospheric Administration (NOAA) (Office for Coastal Management, 2016), and an inventory of coseismic landslides produced during the 1994 M_w 6.7 Northridge Earthquake is available (Harp & Jibson, 1995, 1996). The geologic setting and existing coseismic landslide inventory allow us to leverage both static and dynamic properties of slope stability to evaluate rock strength.

In the study area, surface rock exposures consist of an east to west gradient of progressively older stratigraphic units of a paleo-extensional basin (Figure 1c) (Dibblee, 1991, 1993; Dibblee & Ehrenspeck, 1996).

The age of the exposed strata is, therefore, a proxy for maximum burial depth, and each stratigraphic unit can be viewed as exhumational time steps in the evolution of an inverted basin sequence. The weakly consolidated, shallow-marine to terrestrial Plio-Pleistocene Saugus Formation is predominately a sandstone and pebble conglomerate with clasts sourced from the San Gabriel Mountains, indicating deposition by an ancestral Santa Clara River (DeVecchio et al., 2012; Levi & Yeats, 1993). This unit represents the initial phase of basin inversion and growth of a nascent mountain range. The Pliocene Pico Formation consists of conglomerate, sandstone, and siltstone members deposited in a shallow marine environment (Dibblee, 1993; Yeats et al., 1986). This unit is exhumed from greater depths and represents an intermediate step in the rise of a fault-bounded block. The Monterey (locally known as Modelo) Formation is a deep marine siliceous shale that was deposited throughout much of present-day Southern California during Miocene time (Bramlette, 1946). Within the eastern Topatopa Mountains, this formation was deposited at the paleo-basin margin proximal to its source, resulting in predominately sandstone lithology (Gordon, 2014; Yeats et al., 1994). This unit is exhumed from greater depth and is more strongly lithified than the overlying units, representing the most mature time step in our framework.

Additional constraints on burial histories come from new low-temperature (U–Th)/He thermochronology data. These thermal ages yield constraints on the timing and magnitude of rock exhumation in the eastern Topatopa Mountains because apatite crystals begin retaining radiogenically produced helium after cooling between ~40°C and 80°C (Farley, 2002; Flowers et al., 2009). Assuming a typical geothermal gradient (~15°C/km for sedimentary basins; Ehlers, 2005), the system is sensitive to tectonic and geomorphic processes affecting the upper ~3–5 km of the crust. For detrital grains, such as those preserved in sandstone rocks, the closure temperature must be exceeded during burial in order to release the inherited helium from a previous cooling event and reset the apatite age. Cooling ages that are younger than the stratigraphic age of the rock are assumed to be reset and record a thermal event related to burial and exhumation, whereas cooling ages older than the age of the rock do not record a thermal event related to burial and exhumation. A sample collected from the lowest member of the Monterey fm. in the core of an anticline yielded an apatite cooling age of 3.9 ± 1.2 Ma, which is younger than the stratigraphic age of the rock (Figures 1 and S3, Tables S1 and S2, Supporting Information Text S1). A sample from the highest member of the Monterey fm. in the core of a syncline yielded an apatite cooling age that is older than the stratigraphic age of the rock, and a sample collected from an intermediate member yielded grains that are both younger and older than the age of the rock. These data indicate that only the deepest section of the Monterey fm. experienced complete thermal resetting and thus at least 3 km of burial prior to exhumation. As the Pico and Saugus fms. are stratigraphically higher than the Monterey fm., these must have experienced less burial prior to being exhumed.

2.3. Hillslope Soils and Weathered Rock Profile

Hillslopes in the eastern Topatopa Mountains are partially soil mantled, with soil map regions classified as up to 50% exposed bedrock (Natural Resources Conservation Service, 2019). Where present, soils on these hillslopes are predominately entisols with thin A horizons directly above residuum parent material (Calleguas and Saugus soil series) or inceptisols with weakly developed B horizons (Castaic soil series). Coseismic landslides produced during the 1994 M_w 6.7 Northridge Earthquake predominately originated from ridge tops, where soils and the collective mobile regolith layer were likely thinner than is indicated by type-location profiles for each soil series. Field observations and data from the Natural Resources Conservation Service (2019) suggest that depth to nonmobile regolith (weathered to intact bedrock) in C or Cr horizons beneath these soils is typically ~0.2 to 0.8 m (Figure 3d). Landslides during the Northridge Earthquake were typically 1–5 m deep (Harp & Jibson, 1996), indicating that bedrock beneath the shallow mobile regolith layer must have been mobilized in these hillslope failures in addition to the thin soil mantle.

3. Methods

Here we measured apparent near-surface rock strength using two models that relate Mohr-Coulomb strength parameters to hillslope stability. We first back-calculated strength under static conditions using the Culmann limit-equilibrium, two-dimensional, finite-slope model with 2D hillslope morphology measured from a DEM (e.g., Schmidt & Montgomery, 1995). We then inverted the Newmark limit-equilibrium, one-dimensional, infinite-slope stability analysis for strength under dynamic conditions using 1D hillslope

morphology (slope) measured from a DEM, peak ground accelerations estimated for the 1994 M_w 6.7 Northridge Earthquake (Earle et al., 2009; U.S. Geological Survey, 1994) and a coseismic landslide inventory (Gallen et al., 2015, 2017). We applied these two models to 24 regions in the eastern Topatopa Mountains to produce measures of apparent cohesive and frictional strength, and also compared the results to a data set of direct-shear test results on the relevant stratigraphic units (California Department of Conservation, 2002a, 2002b).

3.1. Estimating Hillslope-Scale Rock Strength Using the Culmann Analysis

A common concept in geomorphology is to assume that landscape form (i.e., topography) reflects a steady-state condition, that is, reflecting a balance between forces that uplift mountains, rock strength, and the erosional forces (including gravity) that act to lower the land surface (Hovius et al., 1998; Montgomery, 2001; Willett & Brandon, 2002). Inherent in this view is the idea that the shape of the land surface represents a limit-equilibrium or "critical" state where the driving forces that change topography are in balance with the resistance to such change provided by rock strength. Applied to individual hillslopes and the formation of landslides, one can imagine that the distribution of hillslope heights and gradients throughout a landscape reflect such a balance, in this case, between gravity acting to destabilize the slope and the resistance provided by the rock, regolith, and soil cover (Hovius et al., 1998; Roering et al., 1999; Schmidt & Montgomery, 1995). Although the concept of criticality is a theoretical one, such an assumption allows us to extract features from digital topography that can be interpreted as estimates for minimum strength parameters related to landsliding processes.

Here we applied a static two-dimensional, finite-slope stability model or "Culmann analysis" (Culmann, 1875; Schmidt & Montgomery, 1995) to digital topography to estimate near-surface rock strength from hillslope morphology over small fluvial catchments (~10 km²). The Culmann analysis predicts slope failure for a simple hillslope of a given height and constant gradient, assuming a planar geometry that intersects the ground surface at the toe of the slope in a wedge-shaped geometry (Figure 2a). The analysis produces thin wedge geometries for steep, planar slopes (greater than ~40°), which are similar to observed failures in steep topography during earthquakes (Keefer, 1994) and also matches predictions from more rigorous approaches using log-spiral mechanisms (Ling et al., 1999). We note that our study area in the eastern Topatopa Mountains is dominated by short, steep, planar hillslopes, where the Culmann criteria is most likely to replicate observed landslides. Failure, or slip on the landslide surface, occurs when the ratio of the weight of the landslide mass exceeds the shear resistance of the slip surface (Factor of Safety = 1), expressed in terms of Mohr-Coulomb strength parameters (cohesion and angle of internal friction). Thus, the Culmann analysis can predict the maximum hillslope height for a given slope that is critically stable for a given measure of cohesion (C) and angle of internal friction (ϕ). For values of hillslope gradient (β) that exceed the friction angle ϕ (typically gradients greater than 25–30°), the Culmann model predicts an exponential-like decay in the maximum height of hillslopes as a function of β. In landscape terms, this criterion predicts that the tallest hillslopes of a particular gradient represent a critical state under static conditions, which then can be interpreted in terms of strength parameters of the near-surface (mean depth of 3.7 m, supporting information) profile subject to shallow landsliding. As strength parameters are determined solely from hillslope morphology, the Culmann approach requires only an input DEM, making it advantageous to other hillslope stability approaches and more broadly exportable to other landscapes. Further, the computational efficiency of this approach permits application at spatial scales as large as entire mountain ranges.

3.1.1. Culmann Finite-Slope Stability Model

The Culmann (1875) limit-equilibrium finite-slope stability model assumes wedge-shaped landslides with planar failure surfaces not parallel to the slope face such that the height of the critical hillslope is given by Equation 1 (Figure 2a).

$$H_c = \left(\frac{4C}{\gamma}\right)\left(\frac{\sin(\beta)\cos(\phi)}{1-\cos(\beta-\phi)}\right). \tag{1}$$

The derivation of the Culmann equation yields a second expression (Equation 2) wherein the angle of modeled landslide failure planes is equal to the arithmetic mean of the angle of internal friction and average hillslope gradient (Lu & Godt, 2013).
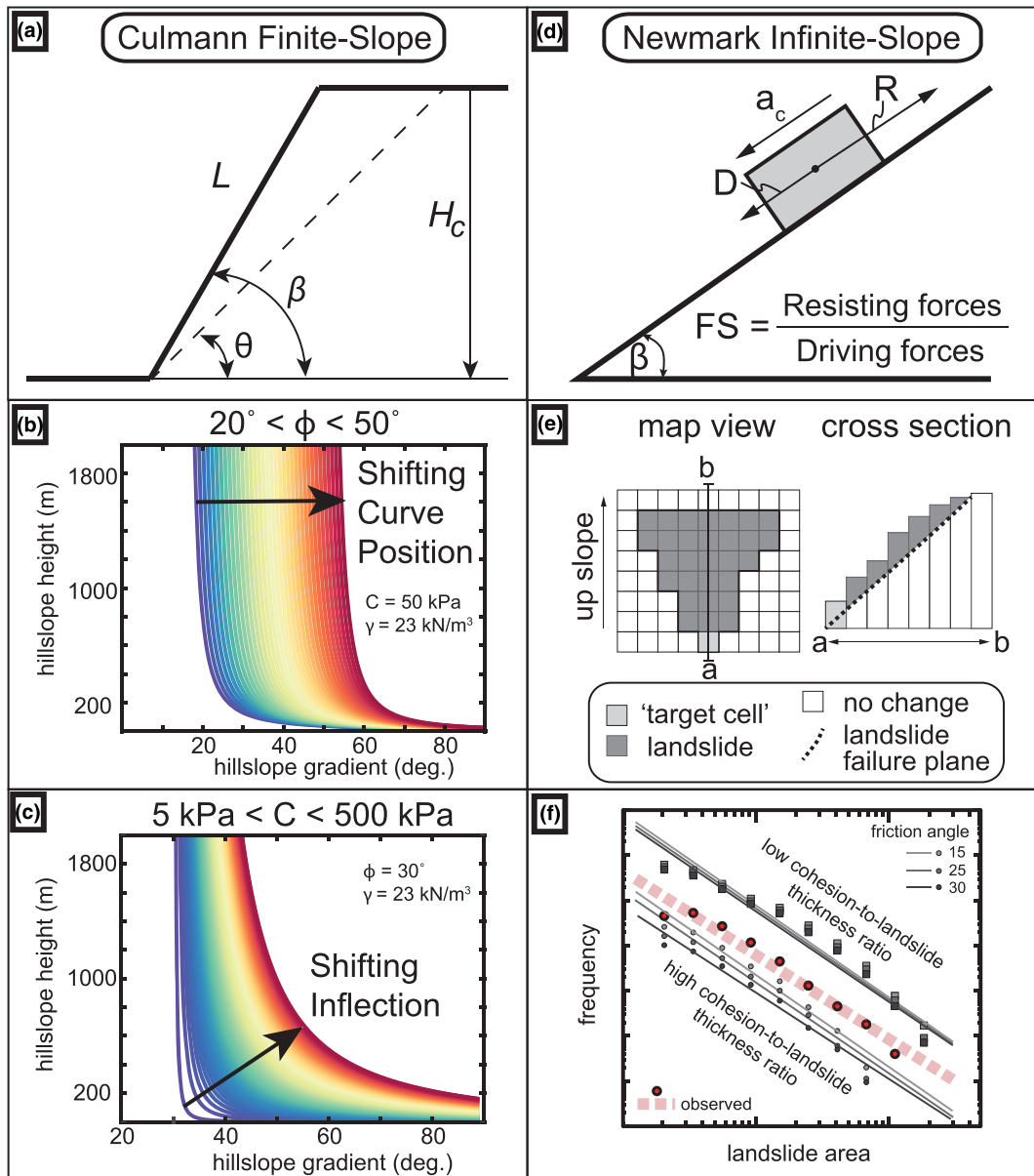
Figure 2. Culmann and Newmark model inputs for strength. (a) Simplified hillslope cross-section with length (L), gradient (β), and critical height (H_c) shown. (b) Theoretical Culmann curves of critically stable hillslope gradients and heights plotted with ϕ increasing in increments of one degree from 20° to 50° while holding c = 50 kPa. (c) Culmann curves plotted with cohesion values increasing in increments of 5 kPa from 5 to 500 kPa while holding ϕ = 30°. (d) Schematic force balance for the factor of safety infinite slope stability solution used on the simplified Newmark method. a_c is the critical acceleration required to overcome basal shear resistance and initiate motion during an earthquake. (e) Illustration of the synthetic landslide geometry used in our simplified Newmark landslide model (after Gallen et al., 2017). (f) An example model result showing the influence of selected cohesion (circles and squares) and internal angle of friction (different shades of gray) on synthetic landslide populations generated by our simplified Newmark landslide model (after Gallen et al., 2015). Solid lines represent best-fit regressions through landslide populations.

$$\theta = \frac{\beta + \phi}{2}. \tag{2}$$

Thus the range of hillslope heights for slope values where $90 > \beta > \phi$ defines a critical relationship between hillslope relief, gradient, and Mohr-Coulomb strength parameters.

Mountainous topography can be parsed into a collection of 2D hillslope segments that extend from a drainage divide to the nearest adjacent channel (Figure 3). We extracted height (H) and average slope (β) for each of these segments within a drainage basin, assumed to be underlain by material of constant strength. This
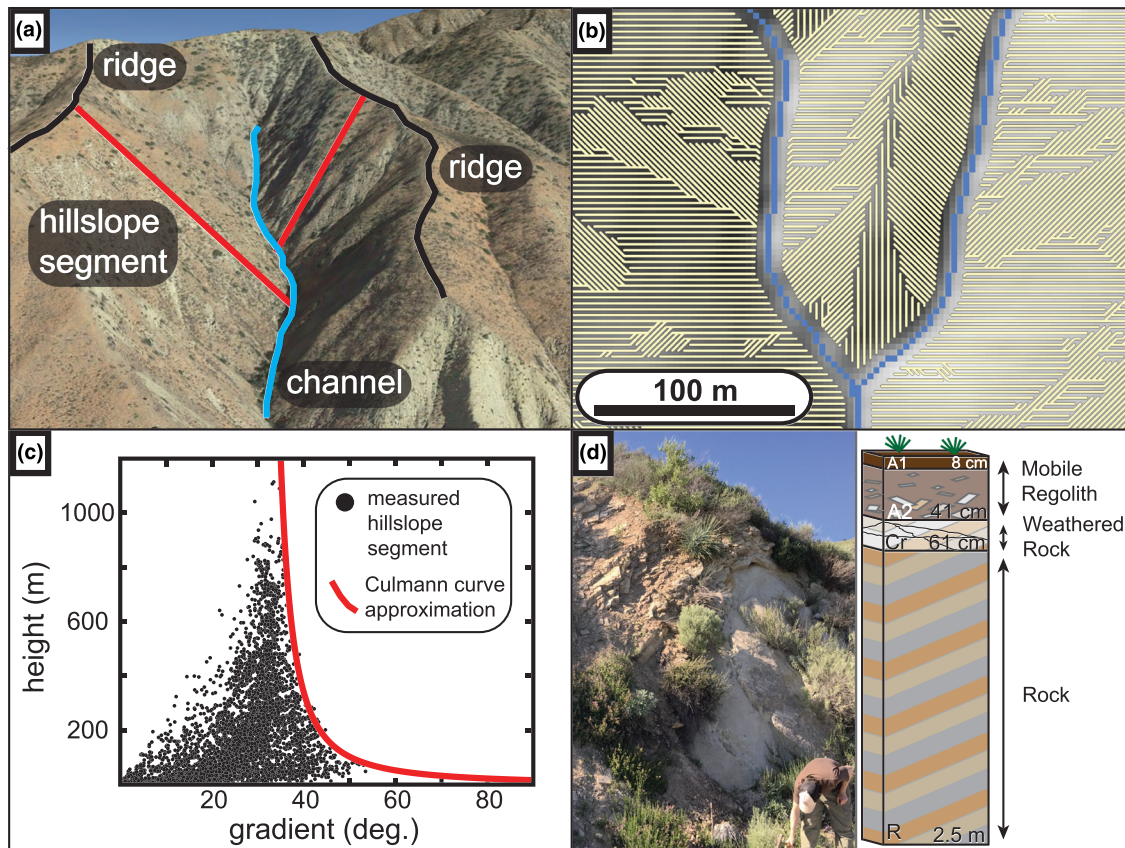
Figure 3. (a) Hillslope flow paths (red) are routed from ridge crests (black) to channels (blue). Imagery from Google Earth. (b) Plan view of modeled hillslope flow paths above the fluvial network produced using GIS workflow. The spacing between flow path centerlines is three meters. (c) Scatter plot of measured hillslope segment gradient (β) versus height (H_C) for a given measurement region. Approximating the threshold of data with the Culmann model results in estimates of cohesion (C) and friction angle (ϕ). (d) Typical profile for hillslope soils in the eastern Topatopa Mountains. Hillslopes are partially mantled by soils, with bedrock commonly exposed at the surface (image). Diagram shows near-surface profile depth over the average thickness of the Northridge coseismic landslides (2.5 m). Where soils are present, depth to weathered bedrock beneath the mobile regolith layer is typically 0.2 to 0.8 m.

analysis produces a scatter plot of H versus β values from which we assert that the envelope encompassing the tallest slopes of various gradients represent the most critical parts of the landscape (the H_c vs. β relationship). Defining this limit requires measuring the height and gradient of many individual hillslope segments (Figure 3).

The Culmann model predicts that threshold hillslope heights exponentially decrease with increasing hillslope gradient; the friction angle estimate is most sensitive to the gradient of the tallest hillslopes while the estimate of apparent cohesion is sensitive to the rate of the exponential decrease in hillslope height with increasing gradient (Figures 2b and 2c). For each measurement region (average of 8.3 km^2), one estimate of C and ϕ is produced, which necessarily assumes that materials characterized by the same strength underlie every hillslope segment within a sampled region. While constant strength is likely not a reality, such an assumption effectively averages strength differences at spatial scales smaller than the measurement region and also likely contributes to some degree of scatter about the H_c versus β relationship.

3.1.2. Hillslope Geometry and Scatter Plots

Here we established a technique to automatically extract hillslope gradient (β) and height (H_c) at intervals equal to the pixel resolution of the input DEM. Standard hydrology raster data sets, including flow direction, flow accumulation, and flow length, were first generated using a NOAA Interferometric Synthetic Aperture Radar (IfSAR) DEM with 3-m pixel resolution (Office for Coastal Management, 2016). We used the D8 algorithm to determine flow direction, in which flow is distributed in 45° azimuth angles to the lowest elevation of the adjoining eight cells (Tarboton et al., 1991). Although it has been argued that the resulting flow paths

do not reflect the dispersive nature of overland flow on hillslopes (Tarboton et al., 1991), this approach allowed us to isolate ridge-to-channel segments into 2D profiles (Figures 3a and 3b). From these raster data sets, flow lines initiating on ridge tops were produced. Hillslope flow lines were isolated from the fluvial network with slope-area analysis, using the contributing area at which the relationship between slope and area switches from a positive to negative trend as a proxy for the transition between hillslope and channelized (debris flows) process domains (Dietrich et al., 2003; Grieve et al., 2016; Montgomery, 2001; Montgomery & Foufoula-Georgiou, 1993; Roering et al., 2007). Although it has been argued by other authors (e.g., Stock & Dietrich, 2003) that the rollover in slope-area space may instead reflect the transition from debris-flow dominated channels to fluvial channels, thereby potentially masking the hillslope-to-channel transition, changing this value by a few tens of square meters does not significantly change the distributions of hillslope geometries. Individual hillslope flow lines were amalgamated at intersections to produce segments that span the entire ridge-to-channel distance. Horizontal flow length and relief across each hillslope segment were extracted, from which the average gradient of the hillslope segment was calculated. In reality, not every hillslope in the landscape is planar, and this approach produces lower gradients for hillslopes with convex profiles than would be identified on a pixel-by-pixel basis. However, as these hillslopes plot at gradients below the threshold in hillslope height versus gradient space, they do not change the strength results.

We sought to create measurement regions small enough to analyze spatial variability in material strength, but just large enough to generate sufficient data to populate the threshold and fit the Culmann curve. We defined regions of 3 to 10 km^2 for high-resolution (3-m or finer) DEMs based on trial and error. To avoid truncating hillslope segments, measurement region boundaries were defined by watershed boundaries. Scatter plots containing hundreds to thousands of (β, H_c) pairs representing individual hillslope segments were created for each measurement region (Figures S5–S28).

3.1.3. Calculating Apparent Cohesion and Friction Angle From the Culmann Model

Assuming uniform strength for small catchment areas, we approximated the threshold in hillslope height versus gradient data with the Culmann model. This analysis produces an estimate of hillslope-scale C and ϕ for each small catchment while holding unit weight (γ) constant at 23 kN/m^3 (Figure 3c). For typical values of γ for a sandstone (20–25 kN/m^3), the resultant C varies by <15%, and ϕ varies by up to one degree, but in the absence of local data, we hold this variable constant. The vast majority of hillslope data plot at relatively low heights and gradients, and each threshold is typically defined by less than 5% of hillslope segments within each catchment. Hillslope data from several basins produced thresholds that are variably well defined with respect to the Culmann model (i.e., the height of the tallest hillslope regularly decreases with increasing slope angle), with some regions yielding data with a larger number of tall moderately steep hillslopes than anticipated by a Culmann model. Curve fitting routines that minimize misfit by eliminating or penalizing static failures (points to the right of the curve) tend to systematically produce unrealistically high friction values because of the relatively few data points for the tallest hillslopes and the large scatter at moderately steep slopes (50–70°) (Figure S31). Instead, the data were fit by inspection by first prioritizing fit to the tallest hillslopes (typically at intermediate gradients of ~30°-50°) followed by fitting the steepest hillslopes, which are typically short (>70° and less than ~20-m height) in order to minimize the number of points to the right of the model curve. By such an approach, nearly every basin has some hillslope data which fall to the right of the model curve. As such, estimated uncertainty in apparent cohesion is estimated to be as high as a few tens of kPa in basins with high C, whereas it may only be a few kPa in basins with low C.

3.2. Newmark Infinite-Slope Stability Inversion for Strength

Following the approach of Gallen et al. (2015), we estimated near-surface material strength under dynamic conditions by inverting a one-dimensional infinite slope stability model that predicts hillslope failure during seismic shaking (simplified Newmark model) with peak ground accelerations, pixel slope, and a coseismic landslide inventory (Jibson, 2007). The simplified Newmark model assumes an infinitely long, planar hillslope and predicts landslide failure cells given local topographic slope, PGA, and rock strength. To turn the resultant distribution of landslide failure cells into a synthetic landslide inventory, we coupled the simplified Newmark analysis with a three-dimensional model of landslide geometry to produce area and volume estimates for each landslide failure. Using an observed landslide distribution during an earthquake event, we inverted these seismic landslide models for near-surface material strength over a spatial window defined from tributary drainage basins (Figure 1) (Gallen et al., 2015).

3.2.1. Seismic Slope Stability and Synthetic Landslide Geometries

The simplified Newmark seismic slope stability analysis is based on the effect of horizontal accelerations during an earthquake acting on a hillslope with static properties (inclination or slope, and the subsurface material properties of soil and rock). Although seismic slope stability analyses have been developed assuming rotational failure planes (e.g., Sarma, 1981), here we applied the simplified Newmark rigid block approach, as coseismic landslides produced during the Northridge earthquake were generally shallow and planar (e.g., Jibson, 2007). Initially, we calculated the static factor of safety of a rigid block with finite thickness using local topographic slope, shear strength (cohesion and the angle of internal friction), density of hillslope material (assumed 2,300 kg m^{-3}), and landslide thickness (Jibson, 1993; Jibson et al., 2000) (Figure 2d). Following Jibson et al. (2000) and Dreyfus et al. (2013), we neglected pore water pressure because the Northridge earthquake occurred during an abnormally dry period, when the transient effects of an elevated water table were likely negligible (Los Angeles Almanac, 2019; Parise & Jibson, 2000). The static factor of safety was calculated for each grid cell in the digital elevation model, as was the horizontal acceleration needed to overcome shear resistance to produce displacement of that block (critical acceleration, or a_c). Using the simplified Newmark analysis, the ratio of peak ground acceleration to the critical acceleration was used to calculate permanent displacements (D_N) experienced over an earthquake based on an empirical relationship (Jibson, 2007), where threshold displacements in excess of 5 cm in the model are identified as slope failure (Godt et al., 2008; Wieczorek et al., 1985).

A simplified Newmark analysis alone is one-dimensional and produces a binary map of grid cells that are identified as either stable or unstable based on an assigned threshold displacement (D_N). To synthesize individual landslide geometries, we assumed that Newmark failure cells ($D_N \geq 5$ cm) are incipient failure points (unstable cells) from which we applied a set of geometric rules to calculate the location and 3D volume of each landslide. From a failure grid cell, we projected a failure plane upslope from a point at depth assuming the slope of the failure plane to be equal to the topographic gradient of the failure grid cell and for the full 3D landslide geometry to be defined from the failure plane projection that daylights at the Earth's surface (Figure 2e, Figure S30, and Text S4) (Gallen et al., 2015). We tested initial point depths ranging from 1.0 to 2.5 m but found that this had little effect on the final strength results (<4 kPa difference). Here we report results using an initial point depth of 2.5 m as this approximates the mean thickness of the 1994 M_w 6.7 Northridge Earthquake coseismic landslides (Harp & Jibson, 1996). From these landslide geometries, we generated synthetic landslide frequency-area distributions (Figure 2f). While lacking a mechanical basis, this simple geometric approximation applied to digital topography produces synthetic landslide distributions that closely match observed power-law scaling of landslide frequency-area statistical distributions for intermediate to large landslides (Gallen et al., 2015).

3.2.2. Inverse Approach

We used a Markov-Chain Monte Carlo routine to invert models generating synthetic landslide populations compared to mapped landslide inventory in order to determine the best-fit strength parameters. For model inputs, we use the local topographic slope (derived from a DEM), and PGA (Earle et al., 2009; U.S. Geological Survey, 1994). Because landslide thickness, cohesion and friction angle collectively contribute to the one-dimensional infinite slope stability factor of safety, we cannot independently solve for these variables. For comparison with results produced with the finite-slope approximation, we set the friction angle using values determined from the Culmann method for each subbasin. Thus, we varied the cohesion-to-thickness ratio (c/t) for each successive model run and then used the modeled landslide geometry to determine the average landslide thickness and express our modeling results in terms of apparent cohesion. The inversion works by maximizing the goodness-of-fit between observed and modeled landside frequency-area statistics over a predefined area (Figure 2f).

3.2.3. Landslide Inventory Remapping

The earthquake-triggered landslide model used in this study is sensitive to the total frequency and size (e.g., area) statistics of landslide populations, and therefore is sensitive to mapping artifacts such as amalgamation (Marc & Hovius, 2015). We remapped a portion of the original Northridge coseismic landslide inventory (Harp & Jibson, 1995) to remove the effects of amalgamation, to relocate misplaced landslides, and to remove anomalously large landslide polygons that contained a mix of disturbed and undisturbed regions (Figure 4; Marc & Hovius, 2015). Further descriptions of our landslide mapping approaches are given in the Supporting Information. Through this effort, we identified 5,064 landslides in the eastern Topatopa
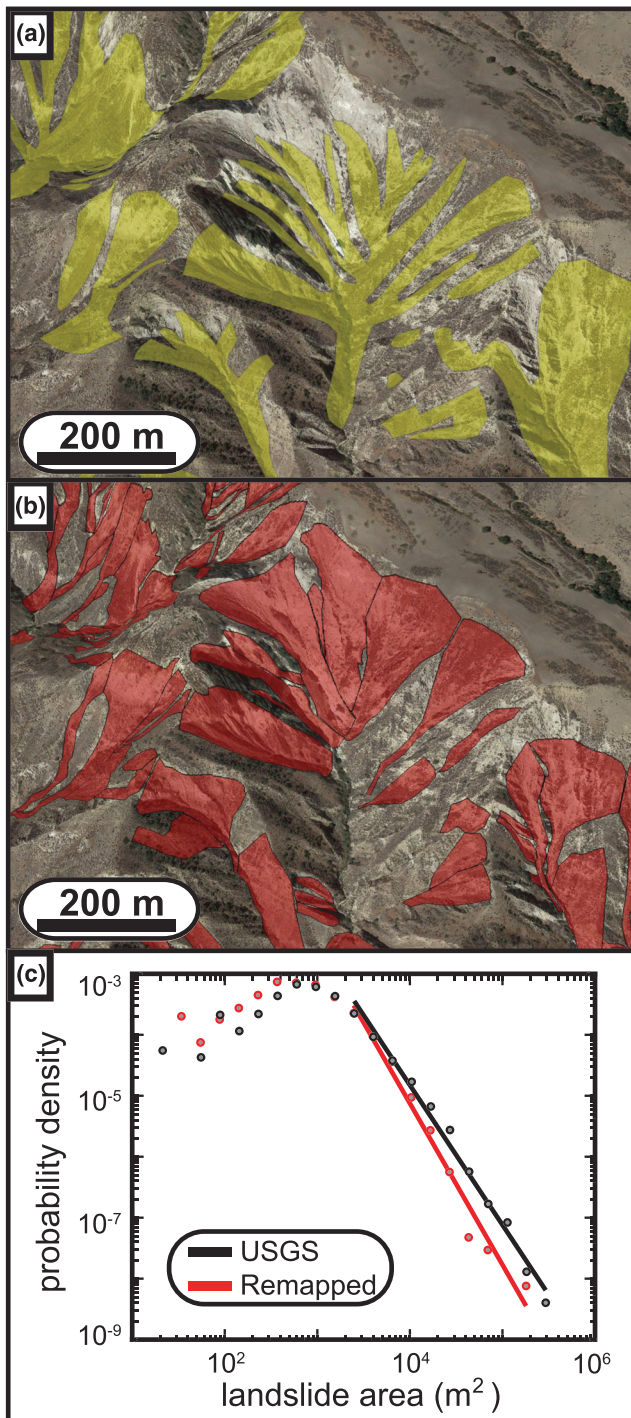
Figure 4. (a) Amalgamated landslide polygons in the original USGS 1994 M_w 6.7 Northridge Earthquake coseismic landslide inventory (Harp & Jibson, 1995, 1996). (b) Remapped landslides in the same extent as "A." (c) Frequency-area scaling of original USGS (black) and remapped (red) landslides. Remapping steepened the regression in log-log space.

Mountains in the region where the original Northridge coseismic landslide inventory contained 3,428 landslides. The remapped inventory has a power-law exponent of −2.65, compared to the original −2.29, effectively steepening the power-law tail of the frequency-area distribution (Figure 4c). Landslide polygons include both scar and runout areas, as the resolution of the historical imagery is too coarse to differentiate between the two.

4. Results

4.1. Modeled Landslide Depths

Landslide depths were calculated as the average distance between the failure plane and landslide surface, normal to the failure plane. The mean landslide depth as predicted by the Culmann model for critically stable hillslopes is 3.7 m (Supporting Information Text S3), and the mean landslide depth of synthetic landslides produced using the Newmark approach is 3.0 m (excluding outliers >20 m thick). These values are within the range of failure plane depths for landslides produced by the 1994 M_w 6.7 Northridge Earthquake, which were typically 1–5 m deep (Harp & Jibson, 1996). Despite the shallow depths of these failures, soil depth on hillslopes in the eastern Topatopa Mountains is generally thin (0.4–0.8 m; Natural Resources Conservation Service, 2019), indicating that bedrock must have been detached in these failures. We, therefore, expect a direct relationship between the strength of the failed material and the underlying rock mass properties, and we cast our strength results in terms of the strength of the rock mass rather than the thin overlying mobile regolith layer. We recognize that the failure plane of landslides assumed by the Culmann model would pass through the mobile regolith zone at the uppermost of lowermost portions of the wedge, but these constitute a minor component of the landslide failure plane. We take results from the Culmann analysis to reflect the average strength of the material underlying each hillslope, which is predominately shallow bedrock.

4.2. Hillslope Data and Culmann Strength Estimates

Scatter plots of hillslope gradient and hillslope height for most watersheds produced a maximum value of slope height/gradient beyond which no hillslopes are measured (Figures 3 and 5). Maximum hillslope heights decrease exponentially with increasing hillslope gradient at angles greater than the tallest hillslope segment, which is consistent with the concept of critical hillslopes predicted by the Culmann failure criterion. Threshold hillslope segments appear distributed throughout most watersheds, but generally, the shorter, steeper critical hillslopes are located above low stream-order channels at the highest elevations, and the tallest critical hillslopes are located above higher stream-order channels at lower elevations (Figure S29). We observe that the density of hillslope segments is typically highest at low gradients and heights, well below the threshold (Figures S5–S28).

Apparent cohesion estimates from individual basins produced by the Culmann model range from 3 to 60 kPa, while friction angle estimates range from 24° to 44° (Figures 5, 6a, and 6c; Table S3). These values are low but consistent with other measurements of hillslope-scale strength (Gallen et al., 2015; Schmidt & Montgomery, 1995). When divided into respective stratigraphic units, we observe that mean friction values overlap within one standard deviation, whereas apparent cohesion values increase with increasing stratigraphic age (Table 1). The Pliocene/Pleistocene Saugus fm. underlying the easternmost basins is the stratigraphically highest unit in the Topatopa Mountains, and these regions produce a mean cohesion estimate of 6 ± 3 kPa (weighted by
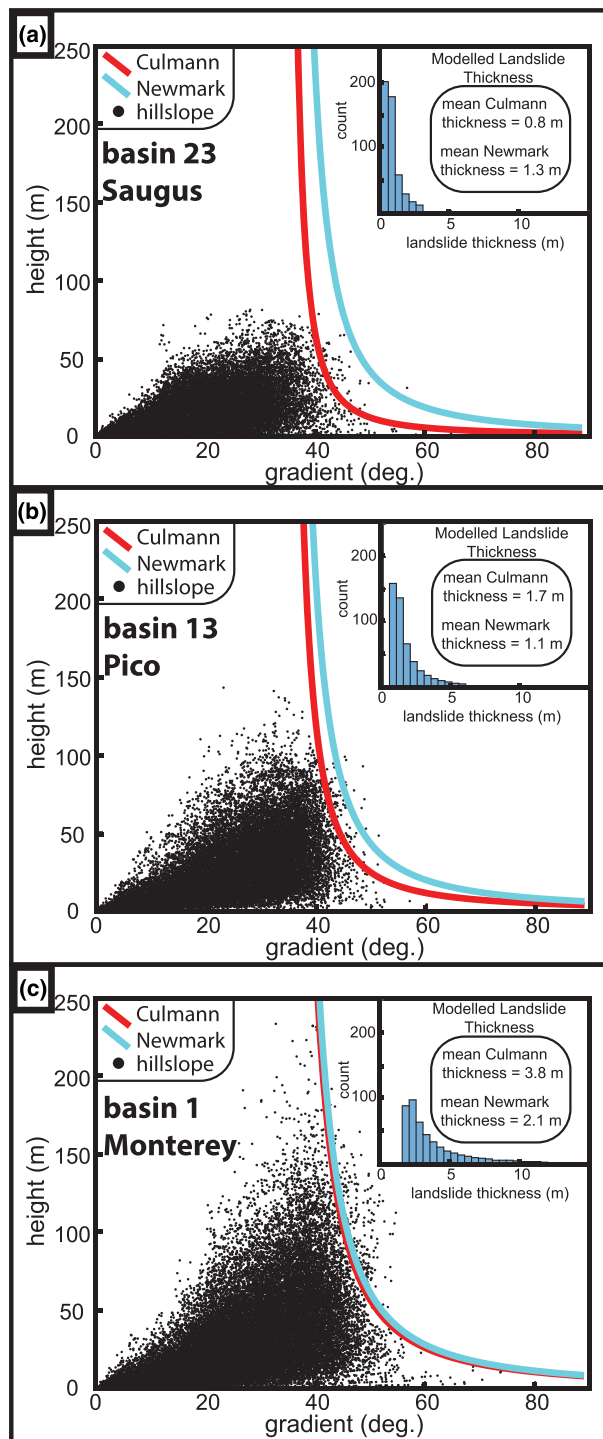
Figure 5. Hillslope segment gradient and height pairs from (a) the Saugus Formation, (b) the Pico Formation, and (c) the Monterey Formation. An exponential decay in hillslope height with gradient from the tallest hillslopes was used to infer strength with the Culmann model (red line). Culmann model curves with cohesive strength set by the Newmark model results are shown in blue. Newmark cohesion values were obtained using friction angle estimates derived from the Culmann analysis from each basin. Inset figure in each panel shows distribution of modeled Culmann landslide thicknesses for hillslope segments that fall along the threshold.

area, with one standard deviation uncertainty) and friction angle of $34 \pm 3°$. Mean cohesion and friction angle of regions overlying the Pliocene Pico fm. to the west of the Saugus fm. basins is 17 ± 13 kPa and $35 \pm 6°$, respectively. The Miocene Monterey fm. exposed in the westernmost basins is the stratigraphically lowest unit, and mean cohesion and friction angle estimates are 40 ± 16 kPa and 31 ± 3 degrees, respectively (Tables 1 and S3). Taken collectively, estimates of apparent cohesion across the three transects increase from east to west as stratigraphically lower units are progressively exposed at the surface due to recent movement on the San Cayetano Fault (Figures 1c and 6a). Friction angle estimates for individual basins generally decrease from east to west with exposure of progressively deeper strata (Tables 1 and S3).

4.3. Newmark Inversion

For the same individual basins used in the Culmann analysis, we considered the frequency-area relationship for the remapped Northridge landslides and compare these to our modified Newmark analysis. We did not apply a scar area correction to the remapped landslides (e.g., Marc et al., 2018) because the minimum size landslide we can model is controlled by the DEM resolution, and applying a scar correction therefore reduces the number of landslides that we can model. Our inverse approach is sensitive to the total number of landslides in each basin, and because full landslide areas were used, recovered strength estimates represent conservative values. For each subbasin, we used the friction value from the Culmann results for that same basin and determine a best-fit c/t value (Figure 2f). We then used the median model thickness for the whole data set (2.2 m) to determine apparent cohesion values for individual basins. These results suggest apparent cohesion from 6 to 30 kPa for friction angles of 24° to 44° (Figure 6b, Table S3) for the entire study area. The mean of cohesion estimates for the Monterey fm. is 26 ± 3 kPa, the Pico fm. is 16 ± 5 kPa, and the Saugus fm. is 15 ± 3 kPa (Tables 1 and DR3). Variability in the quality of fits between synthetic and observed frequency-area distributions is likely driven by a mismatch between the topography that is predicted to landslide and the topography that actually failed in landslides during the earthquake (Supporting Information Text S5).

Overall, the Newmark and Culmann estimates both produced low values of apparent cohesion (tens to several tens of kPa) and differ by up to ~10 kPa for averages within the same stratigraphic units (Figure 7, Table 1). The Newmark results produced a correlation between apparent cohesion and stratigraphic age between the Monterey and Pico fms., but did not distinguish values between the Pico and Saugus fms. The Newmark results estimated higher (+9 kPa) mean cohesive strength of the Saugus fm. compared to the Culmann model, while Newmark and Culmann mean estimates of cohesive strength are identical for the Pico fm. (within 1 kPa) (Table 1). The Newmark model produced a lower mean (−14 kPa) estimate of cohesion for the Monterey fm. compared to the Culmann model (Table 1). The basins with the greatest disagreement in cohesion estimates do not appear to be a result of either poor Newmark fits and poorly defined thresholds for the Culmann curve (Supporting Information Text S5).

4.4. Laboratory Strength Estimates

We compared laboratory direct-shear tests published by the California Geological Survey to our model results in order to evaluate the difference between hand-sized samples and more integrative estimates provided by the
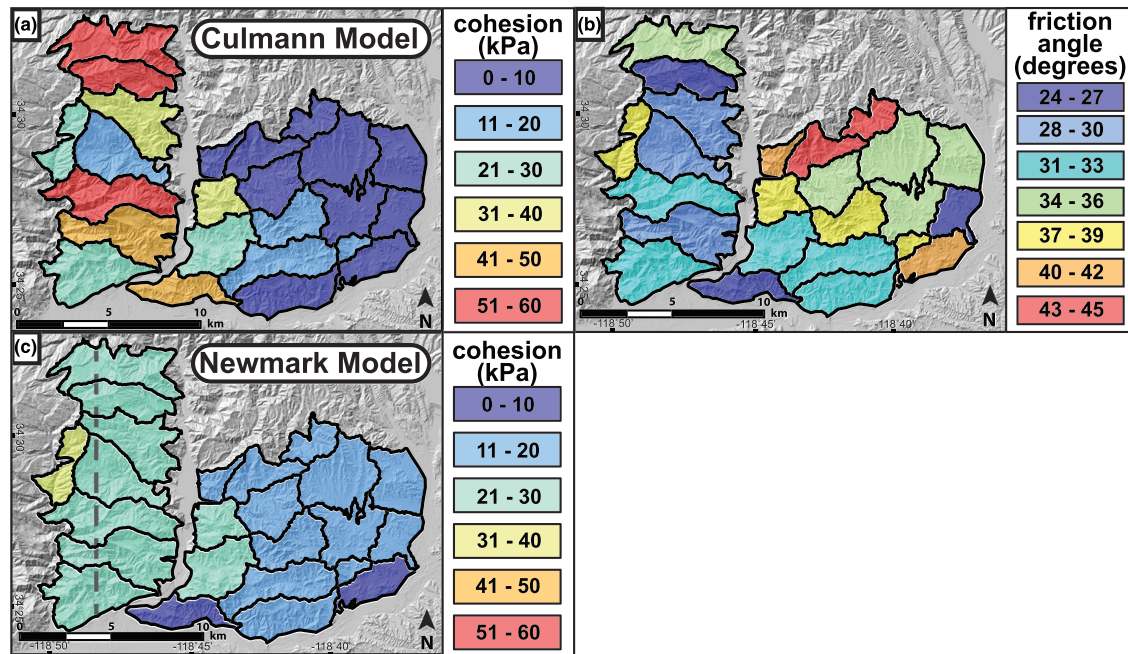
Figure 6. Map view of strength results. (a) Cohesion (kPa) produced from the Culmann finite-slope stability model, (b) friction angle (degrees) produced from the Culmann model, and (c) cohesion produced from inversion of the Newmark infinite-slope stability model. Cohesion results from the Newmark model were calculated using friction angle estimates derived from the Culmann analysis for each basin. Dashed line shows location of strength transects and geologic cross section in Figure 9.

stability models. Notably, we expect that laboratory-based measurements do not capture fractures and other discontinuities that may penalize strength values at the hillslope scale; thus, we generally should expect the stability-based models to yield lower strength estimates compared to direct-shear tests. Samples were collected from boreholes and excavations, and direct-shear tests were conducted on unconsolidated, saturated samples under drained conditions. Reported cohesion and friction angles reflect peak strength required to induce failure of the sample. Data were filtered to remove samples collected from soils or landslide deposits. Direct-shear tests of three samples from the Monterey fm. yield a mean cohesion of 51 ± 32 kPa and mean friction angle of $33 \pm 3°$ (Figure 7, Table 1) (California Department of Conservation, 2002a, 2002b, 2018). Direct-shear tests from 14 samples in the Pico fm. yield a mean cohesion of 27 ± 15 kPa and friction angle of $34 \pm 7°$, and direct-shear tests from 79 Saugus fm. samples yield mean cohesion of 30 ± 26 kPa and friction angle of $34 \pm 7°$ (Figure 7, Table 1). It should be noted that the samples for direct-shear tests were collected from the associated stratigraphic units in the vicinity of our 24 study regions for model strength estimates, but not necessarily from within them (Figure S2).

In comparison between model-driven and direct-shear tests, there is consistency across both methods and stratigraphic units around a friction value of ~$32 \pm 5°$. Variability in cohesion is greater, although still within

Table 1
Average Estimates of Cohesion and Friction Angle (± 1 Standard Deviation) From the Culmann Model, Newmark Model Inversion, and Direct-Shear Tests on Hand Samples

	Monterey formation		Pico formation		Saugus formation	
	C (kPa)	ϕ (degrees)	C (kPa)	ϕ (degrees)	C (kPa)	ϕ (degrees)
Culmann model	40 ± 16	31 ± 3	17 ± 13	35 ± 6	6 ± 3	34 ± 3
Newmark model	26 ± 3	-	16 ± 5	-	15 ± 3	-
Direct-shear test[a]	51 ± 32	33 ± 3	27 ± 15	34 ± 7	30 ± 26	34 ± 7

Note. Culmann and Newmark averages are weighted by basin area.
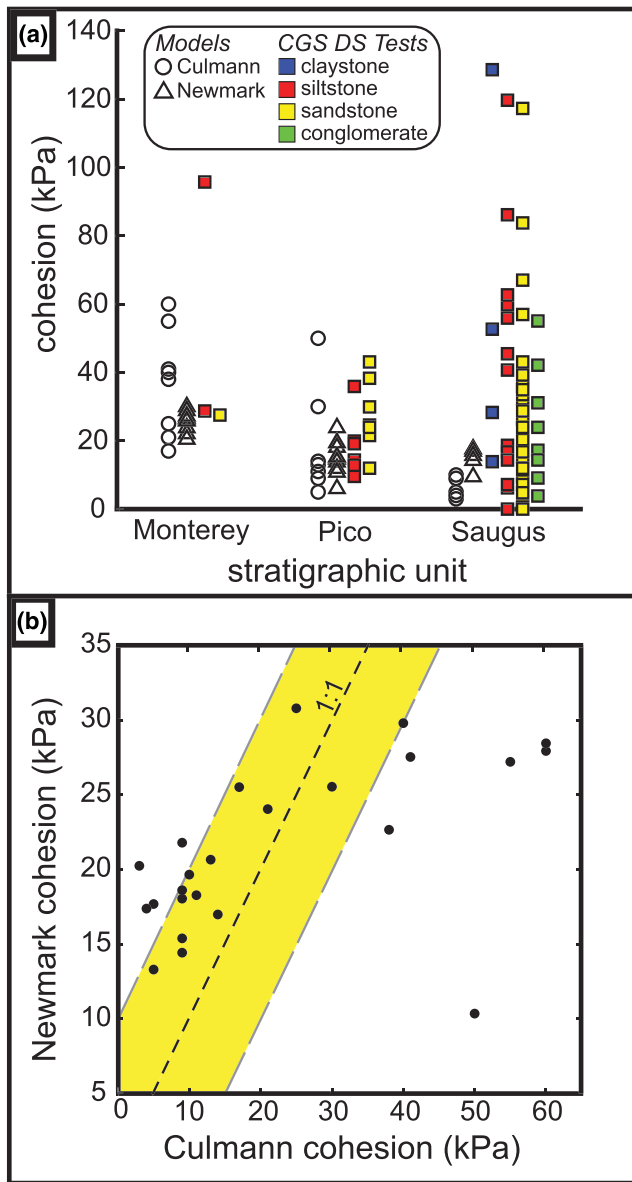[a]Source: California Department of Conservation seismic hazard reports (2002a, 2002b).

Figure 7. (a) Cohesive strength of the Saugus, Pico, and Monterey Formations from each basin by the Culmann and Newmark models. California Geological Survey (CGS) direct-shear (DS) test data are separated by lithology within each unit. (b) Newmark model cohesion results plotted against Culmann model cohesion results. Yellow shaded region shows ±10 kPa from one-to-one relationship (black dashed line).

a fairly narrow range of values (several tens of kPa, Figure 7). Direct-shear tests are on average higher for all three formations compared to the Culmann and Newmark values. Despite the large range in direct-shear test results, the cohesive strength of the weakest rocks from each unit systematically decreases from ~28 kPa in the Monterey fm., to ~10 kPa in the Pico fm., to 0 kPa in the Saugus fm. (Figure 7a). These values are similar to mean results produced from the slope stability model approaches.

4.5. Burial Depth

The three stratigraphic units in the eastern Topatopa Mountains exhibit a gradient in maximum burial depth from east to west. The Saugus fm. is the stratigraphically highest unit in much of the Western Transverse Ranges, and with the exception of minor latest-Pleistocene to Holocene alluvial fills, has not been buried by overlying section (DeVecchio et al., 2012). Subsurface data suggest that the maximum thickness of the Saugus fm is ~2,040 m in the easternmost Topatopa Mountains (Dibblee, 1996), the maximum thickness of the Pico fm. is ~2,000 m (Dibblee, 1993, 1996), and the maximum thickness of the Monterey fm. is ~2,500 m (Gordon, 2014; Yeats et al., 1994). Using these thicknesses and structural data in published geologic maps (Dibblee, 1991, 1993, 1996; Dibblee & Ehrenspeck, 1996, 1997), we estimated the minimum and maximum burial depth of rocks exposed within each measurement region (Table S4), assuming that the thickness of each unit was originally constant. We recognize that there is significant variability in the thickness of the Saugus fm. where preserved elsewhere (e.g., DeVecchio et al., 2012), but an assumption of constant thickness over our study area is appropriate in the absence of local data. As expected, burial depth generally increases from east to west (Table S4). Cohesive strength results from both the Newmark and Culmann models increase with increasing burial depth, both within and between formations (Figure 8).

5. Discussion
5.1. Difference in Model Strength Results

Strength results from the Newmark and Culmann approaches are generally in good agreement, with 60% of the basins producing results within 10 kPa for comparative apparent cohesion values (recall that the Newmark method does not produce independent cohesion/friction results) (Figure 7b). When comparing Newmark fits against the height-slope data used to fit the Culmann model, the Newmark values still fall within the scatter of height-gradient values despite being independent of these data (Figures S5–S28). However, these fits variably hug the outliers of the height-slope data or lie within a scatter of low-density data (Figure 5). Here we notice two particular trends. First, at cohesion below 25 kPa, the Newmark model predicts higher estimates than the Culmann model (following the most extreme height-slope values), while at cohesion greater than ~25 kPa, the Newmark model produces estimates that are lower than the Culmann model and lie within the low-density region of height-gradient data (Figure 7b). The low cohesion basins have substantially lower median slope values compared to the higher cohesion values, reflecting the influence of strength on hillslope morphology (Korup, 2008). Also, these lower modal values for average hillslope gradient are associated with a less-defined peak in height-gradient values (Figure 5a vs. Figure 5c) (Figures S5–S28). Certainly, values within 10 kPa may be considered well within error of our curve-fitting approach for the Culmann method, given the relatively high scatter in the hillslope distributions for some basins. The fact that the Newmark method produces such similar results supports the hypothesis that near-surface rock
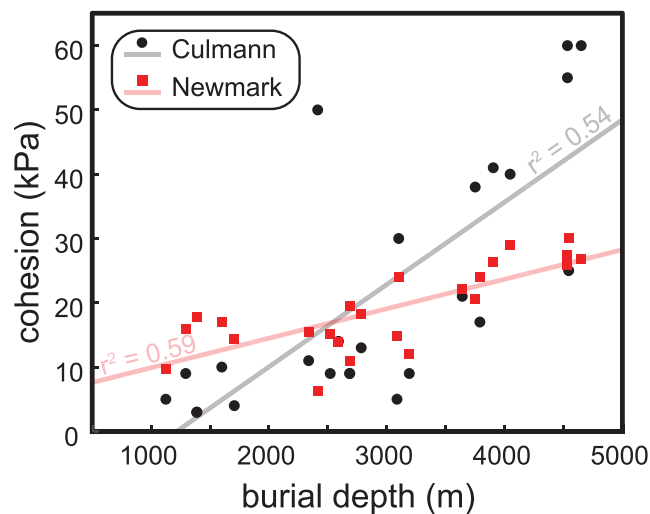
Figure 8. Culmann and Newmark cohesion results against average burial depth of sedimentary rocks within each measurement region. Solid lines show best-fit regressions.

strength may be faithfully recorded in the topographic structure, but we acknowledge that a statistical measure to quantify uncertainty would further support this interpretation.

The alternative explanation for some of the higher scatter (~10- to 30-kPa difference) is that the differences in strength instead reflect a difference in model assumptions or hillslope processes. Basins with the highest disagreement overlie the Monterey fm., which commonly consists of alternating beds of massive sandstone and shale. We observe that sandstone beds are often undercut and protrude out of steep anti-dip slopes relative to shale beds, and shallow coseismic landslides and rockfalls during the 1994 M_w 6.7 Northridge Earthquake were common on these hillslopes. However, these hillslopes are also generally taller and steeper than hillslopes underlain by the Pico and Saugus fms. These observations imply that the general morphology of these hillslopes is supported by the stronger sandstone beds, resulting in relatively high apparent cohesion estimates from the Culmann model, but the instability of the overhanging blocks results in lower apparent cohesion values from the Newmark model. Alternatively, we also recognize that a 1D stability model will be more conservative than its 2D counterpart due to a lack of consideration of resisting forces in the second dimension.

The Culmann and Newmark model strength results from each stratigraphic unit are lower than mean direct-shear test results (Table 1). We interpret the lower strength at the hillslope scale as being driven by discontinuity sets within the rock mass that are not captured at the small scale of the laboratory tests (e.g., Hoek & Brown, 1997). However, we also observe that hillslope-scale strength results are similar to the weakest direct-shear test results within each stratigraphic unit (Figure 7a). An alternative explanation is that hillslope-scale strength is instead limited by the strength of the weakest member of a formation within a hillslope (e.g., Schmidt & Montgomery, 1995). A potential mechanism that may be responsible for this pattern is that landslide failure planes localize on the weakest rocks in a hillslope, and strength calculated using hillslope stability models would, therefore, reflect the strength of these units. In this framework, intact rock strength from individual laboratory-sized samples can greatly exceed hillslope-scale strength estimates (e.g., the Saugus fm., Figure 7a), but hillslope-scale strength can generally not exceed the strength of the weakest rocks within a formation.

5.2. Rock Strength Controlled by Burial Depth

Collectively, model and direct-shear tests show increasing cohesion across an east to west gradient with increasing formation age and stratigraphic depth, suggesting the interunit differences in strength may be attributed to maximum burial depth of these units prior to exhumation. Support for the control of burial depth on strength also arises from Culmann estimates of cohesion within the Monterey fm. Variability within this unit can be explained by exposed stratigraphic position within the Temescal anticline and Santa Felica syncline—two multi-kilometer scale folds developed parallel to the main thrust front (Dibblee, 1991; Figure 9). Although the pattern is more subdued in the Newmark apparent cohesion estimates, these also mimic the broad-scale folding and variation in stratigraphic interval (Figure 9). Cohesive strength is highest where the deepest members of the Monterey fm. are exposed in anticlines, and strength is lowest where the highest members are exposed. Low-temperature apatite (U–Th/He) thermochronology data from the Monterey fm. show complete thermal resetting of apatite from the core of the Temescal Anticline, cooling ages older than the formation age of the Monterey fm. near the Santa Felicia Syncline, and partial resetting from intermediate samples (Figure 9, Tables S1 and S2), suggesting that the deepest members of the unit reached a maximum burial depth of at least three kilometers before being exhumed (assuming a geothermal gradient of ~15°C/km for sedimentary basins). These results suggest that maximum burial depth and associated vertical exhumation likely exert a first-order control on the strength of these geologically young stratigraphic units. The lower estimates of strength from the Pico and Saugus fms. are also consistent with this interpretation; although no thermochronology data from these formations have been
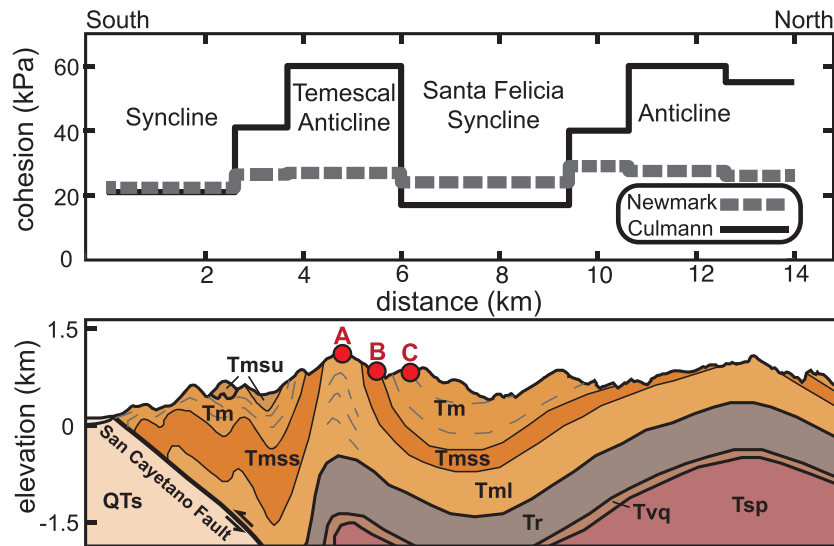
Figure 9. Transect across the Miocene Monterey Formation. Transect location shown in Figures 1a and 6c. Plot shows cohesion estimates from the Culmann model and apparent cohesion results from the Newmark model against distance from the range front (south to north). Lower panel shows a geologic cross section through the Monterey and underlying fms. Modified from Dibblee (1991) and Dibblee and Ehrenspeck (1996). Strength estimates are highest over structural anticlines, where rock exposed at the surface has been exhumed from greater depth. "A" shows location of apatite (U–Th)/He sample 16-PC-4, which was collected from the core of the Temescal Anticline and had been buried deep enough to be thermally reset. "B" and "C" show location of unreset or partially reset ages indicating shallow burial. Geologic unit abbreviations: QTs (Saugus Formation), Tmsu (Monterey Formation, upper sandstone member), Tm (Monterey Formation, lower sandstone members), Tmss (Monterey Formation, sandstone), Tml (Monterey Formation, lower shale unit), Tr (Rincon Shale), Tvq (Vaqueros Sandstone), Tsp (Sespe Formation).

produced, these units are stratigraphically higher than the old, nonreset apatite grains from the upper members of the Monterey fm., suggesting less than 3 km of burial and exhumation.

The gradient in rock strength with stratigraphic age is likely a consequence of differing degrees of lithification and diagenesis associated with burial depth. Young, recently deposited sediments are loosely packed, have high porosity, and are generally uncemented. Continued sediment deposition in a subsiding basin progressively buries older sediments, which experience a concurrent increase in pressure and temperature. Elevated pressures caused by loading drive a significant increase in grain packing and reduction in pore space due to both physical and chemical compaction, which can continue to depths of at least 5 km (Worden & Burley, 2003). Chemical compaction results in the partial dissolution of minerals, which enrich pore water with dissolved silica. Precipitation of this silica and other minerals within the pore space results in cementation, which further reduces pore space and brings about lithification of the sediments (Boggs Jr., 2011). The degree of compaction and cementation associated with varying burial depth exert a strong control on the cohesive strength of sedimentary rocks (Collins & Sitar, 2008). In the Topatopa Mountains, the friable, poorly consolidated condition of the Pico and Saugus fms. is likely a result of minimal compaction due to these units' shallow burial depth. The Monterey fm., by contrast, experienced higher temperatures and pressures due to burial beneath the Pico and Saugus fms. Therefore, the higher degree of diagenesis associated with deeper burial is likely responsible for the higher cohesive strength of the Monterey fm. While these findings are perhaps unsurprising, they remain some of the first to provide quantitative constraints on the potential effects of lithification and diagenesis on landscape-scale strength.

5.3. Other Controls on Hillslope-Scale Rock Strength

Off-fault deformation associated with slip along active faults has been proposed to weaken the surrounding rock mass and potentially influence the distribution of landsliding (Korup, 2004; Scheingross et al., 2013). Along the San Andreas Fault in central California, landslides not otherwise triggered by earthquakes have been observed to cluster within a couple of kilometers of the fault due to a reduction in rock strength

associated with fault-proximal deformation of the surrounding rock mass (Scheingross et al., 2013). If the distribution of rock strength in the Topatopa Mountains were similarly controlled by fault-induced deformation, we should expect a north-south gradient in strength associated with proximity to the range-bounding San Cayetano Fault, which is oriented east-west (Figure 1c). While we cannot discount fracturing due to fault proximity as a control, we clearly see a dominant east-west gradient in strength that mirrors the exposure of sedimentary rocks, suggesting that original burial depth is a stronger control on the distribution of rock strength than deformation driven by local tectonism. Further, variability from north to south also closely mimics anticlinal structure rather than fault proximity within the Monterey fm. (Figure 9).

Other potential factors that influence slope failure or rock mass strength may be correlated with lithologic unit and original burial depth. Given the currently available data sets, we observe a correlation between rock strength and the original burial depth of these young sedimentary rocks, but other variables including porosity, mineralogy, and composition of interstitial cements, weathering controls, hydraulic conductivity, tectonic deformation rate, timing of rock exhumation initiation, and erosion rate may also vary in a systematic way that mirrors the distribution of rock strength. These data sets are currently unavailable in the eastern Topatopa Mountains, so we offer burial depth as a likely dominant control in this unique field setting but acknowledge that these other variables may contribute to the variability in rock mass strength.

6. Conclusions

Here we provide a methodology to quantify rock strength, which is an important control on topographic relief and supports conceptual models for landscape evolution posed by some of the earliest geomorphologists (Davis, 1899; Gilbert, 1877). We estimate hillslope-scale rock strength in the Eastern Topatopa Mountains using the Culmann finite-slope and Newmark infinite-slope stability models. With the Culmann model, we calculate the apparent cohesion and friction angle of hillslope materials by measuring the gradient and height of hillslope segments from a high-resolution (3 m) DEM. By extracting these measurements over a defined measurement region, we estimate strength assuming that the limit in height versus gradient space represents the critical, strength-limited components of the landscape. We invert the Newmark model for strength using local topographic slope, PGA model for the 1994 M_w 6.7 Northridge Earthquake, and the inventory of Northridge coseismic landslide polygons remapped to reduce amalgamation. To directly compare the resulting strength estimates, we fix the friction angle estimates for the Newmark inversion with the Culmann model estimates. Cohesive and frictional strength results from the Saugus fm. using the Culmann approach are 6 ± 3 kPa and $34 \pm 3°$, respectively, where the Newmark predicts a cohesion of 15 ± 3 kPa using the friction angle results from the Culmann. The Culmann model predicts a mean cohesion of 17 ± 13 kPa and friction angle of $35 \pm 5°$ from the Pico fm., where the Newmark approach predicts a mean cohesion of 16 ± 5 kPa. Mean results for the Monterey fm. from the Culmann approach are 40 ± 16 kPa for cohesion and $31 \pm 3°$ for the friction angle, where the Newmark predicts cohesion of 26 ± 3 kPa. The patterns in cohesive strength across the eastern Topatopa Mountains are similar, with strength increasing from east to west with increasing stratigraphic age and depth in Plio-Pleistocene to Miocene clastic sedimentary rocks. Within the Monterey fm., the stratigraphically lowest unit, near-surface strength is highest over the cores of anticlines and lowest over synclines, suggesting that maximum burial depth is a major control on strength in these geologically young, poorly lithified sedimentary rocks.

Data Availability Statement

Our remapped landslide inventory is available at the USGS Open Repository of Earthquake-Triggered Ground-Failure Inventories. Thermochronometry sample data and the California Geological Survey direct-shear test data used in this study are available at the Deep Blue data repository (https://doi.org/10.7302/9bj1-q884). The digital elevation model used in this study is available from the U.S. National Oceanic and Atmospheric Administration at coast.noaa.gov/dataviewer, the original inventory of coseismic landslides produced during the 1994 M_w 6.7 Northridge Earthquake is available from the U.S. Geological Survey at catalog.data.gov, and the Shakemap of peak ground accelerations during the Northridge Earthquake is available from the U.S. Geological Survey (https://earthquake.usgs.gov/). A supplemental document containing a summary of laboratory and analytical protocols for apatite (U–Th)/He

thermochronometry, landslide mapping methods, Culmann model methods, tables with thermochronometry sample information, and supplemental figures is included in the Supporting Information.

References

Atwater, T. M. (1998). Plate tectonic history of southern California with emphasis on the western Transverse Ranges and northern Channel Islands. In P. W. Weigand (Ed.), *Contributions to the geology of the Northern Channel Islands, Southern California* (pp. 1–8). Pacific Section: American Association of Petroleum Geologists.

Boggs Jr., S. (2011). *Principles of sedimentology and stratigraphy*. London, UK: Pearson.

Bramlette, M. N. (1946). *The Monterey Formation of California and the origin of its siliceous rocks* (Report 212). Washington, DC: US Government Printing Office.

Bursztyn, N., Pederson, J. L., Tressler, C., Mackley, R. D., & Mitchell, K. J. (2015). Rock strength along a fluvial transect of the Colorado Plateau—Quantifying a fundamental control on geomorphology. *Earth and Planetary Science Letters*, *429*, 90–100. https://doi.org/10.1016/j.epsl.2015.07.042

California Department of Conservation. (2002a). Seismic hazard zone report for the Piru 7.5-minute quadrangle, Ventura County, California. In *California Division of Mines and Geology Seismic Hazard Zone Report 074* (Vol. 54). Sacramento, CA. https://gmw.conservation.ca.gov/SHP/EZRIM/Reports/SHZR/SHZR_074_Piru.pdf

California Department of Conservation. (2002b). Seismic hazard zone report for the Val Verde 7.5-minute quadrangle, Los Angeles and Ventura Counties, California. In *California Division of Mines and Geology Seismic Hazard Zone Report 076* (Vol. 52, pp. 1–49). Sacramento, CA.

California Department of Conservation. (2018). *Borehole database*. Sacramento, CA: California Geological Survey. https://www.conservation.ca.gov/cgs/maps-data/borehole-database

Collins, B. D., & Sitar, N. (2008). Processes of coastal bluff erosion in weakly lithified sands, Pacifica, California, USA. *Geomorphology*, *97*(3–4), 483–501. https://doi.org/10.1016/j.geomorph.2007.09.004

Culmann, C. (1875). *Die Graphische Statik*. Zurich: Meyer and Zeller.

Davis, W. M. (1899). The geographical cycle. *The Geographical Journal*, *14*(5), 481–504. https://doi.org/10.2307/1774538

DeVecchio, D. E., Heermance, R. V., Fuchs, M., & Owen, L. a. (2012). Climate-controlled landscape evolution in the Western Transverse Ranges, California: Insights from Quaternary geochronology of the Saugus Formation and strath terrace flights. *Lithosphere*, *4*, 110–130. https://doi.org/10.1130/L176.1

Dibblee, T. W. (1991). *Geologic map of the Piru Quadrangle, Ventura County, California* (Map DF-34, scale 1:24,000). Santa Barbara, CA: Dibblee Geological Foundation.

Dibblee, T. W. (1993). *Geologic map of the Val Verde Quadrangle, Los Angeles and Ventura counties, California* (Map DF-50, scale 1:24,000). Santa Barbara, CA: Dibblee Geological Foundation.

Dibblee, T. W. (1996). *Geologic map of the Newhall Quadrangle* (Map DF-56, scale 1:24,000). Santa Barbara, CA: Dibblee Geological Foundation.

Dibblee, T. W., & Ehrenspeck, H. E. (1996). *Geologic map of the Cobblestone Mountain Quadrangle, Ventura and Los Angeles counties, California* (Map DF-62, scale 1:24,000). Santa Barbara, CA: Dibblee Geological Foundation.

Dibblee, T. W., & Ehrenspeck, H. E. (1997). *Geologic map of the Whitaker Peak quadrangle, Los Angeles and Ventura counties, California* (Map DF-63, scale 1:24,000). Santa Barbara, CA: Dibblee Geological Foundation.

DiBiase, R. A., Rossi, M. W., & Neely, A. B. (2018). Fracture density and grain size controls on the relief structure of bedrock landscapes. *Geology*, *46*(5), 399–402. https://doi.org/10.1130/G40006.1

Dietrich, W. E., Bellugi, D. G., Heimsath, A. M., Roering, J. J., Sklar, L. S., & Stock, J. D. (2003). Geomorphic transport laws for predicting landscape form and dynamics. *Geophysical Monograph*, *135*(D24), 1–30. https://doi.org/10.1029/135GM09

Dolan, J. F., & Rockwell, T. K. (2001). Paleoseismologic evidence for a very large (Mw >7), Post-A.D. 1660 surface rupture on the Eastern San Cayetano fault, Ventura county, California: Was this the elusive source of the damaging 21 December 1812 earthquake? *Bulletin of the Seismological Society of America*, *91*(6), 1417–1432. https://doi.org/10.1785/0120000602

Dolan, J. F., Sieh, K., Rockwell, T. K., Yeats, R. S., Shaw, J. H., Suppe, J., et al. (1995). Prospects for larger or more frequent earthquakes in the Los Angeles metropolitan region. *Science*, *267*(5195), 199–205. https://doi.org/10.1126/science.267.5195.199

Dreyfus, D., Rathje, E. M., & Jibson, R. W. (2013). The influence of different simplified sliding-block models and input parameters on regional predictions of seismic landslides triggered by the Northridge earthquake. *Engineering Geology*, *163*, 41–54. https://doi.org/10.1016/j.enggeo.2013.05.015

Earle, P. S., Wald, D. J., Jaiswal, K. S., Allen, T. I., Marano, K. D., Hotovec, A. J., et al. (2009). Prompt Assessment of Global Earthquakes for Response (PAGER): A system for rapidly determining the impact of global earthquakes worldwide. In *U. S. Geological Survey Open-File Report 2009-1131* (pp. 1–15). Reston, VA.

Ehlers, T. A. (2005). Crustal thermal processes and the interpretation of thermochronometer data. *Reviews in Mineralogy and Geochemistry*, *58*(1), 315–350. https://doi.org/10.2138/rmg.2005.58.12

Farley, K. A. (2002). (U-Th)/He dating: Techniques, calibrations, and applications. *Reviews in Mineralogy and Geochemistry*, *47*(1), 819–844. https://doi.org/10.2138/rmg.2002.47.18

Flowers, R. M., Ketcham, R. A., Shuster, D. L., & Farley, K. A. (2009). Apatite (U-Th)/He thermochronometry using a radiation damage accumulation and annealing model. *Geochimica et Cosmochimica Acta*, *73*(8), 2347–2365. https://doi.org/10.1016/j.gca.2009.01.015

Forte, A. M., Yanites, B. J., & Whipple, K. X. (2016). Complexities of landscape evolution during incision through layered stratigraphy with contrasts in rock strength. *Earth Surface Processes and Landforms*, *41*(12), 1736–1757. https://doi.org/10.1002/esp.3947

Frattini, P., & Crosta, G. B. (2013). The role of material properties and landscape morphology on landslide size distributions. *Earth and Planetary Science Letters*, *361*, 310–319. https://doi.org/10.1016/j.epsl.2012.10.029

Gallen, S. F. (2018). Lithologic controls on landscape dynamics and aquatic species evolution in post-orogenic mountains. *Earth and Planetary Science Letters*, *493*, 150–160. https://doi.org/10.1016/j.epsl.2018.04.029

Gallen, S. F., Clark, M. K., & Godt, J. W. (2015). Coseismic landslides reveal near-surface rock strength in a high relief, tectonically active setting. *Geology*, *43*(1), 11–14. https://doi.org/10.1130/G36080.1

Gallen, S. F., Clark, M. K., Godt, J. W., Roback, K., & Niemi, N. A. (2017). Application and evaluation of a rapid response earthquake-triggered landslide model to the 25 April 2015 Mw 7.8 Gorkha earthquake, Nepal. *Tectonophysics*, *714*, 173–187. https://doi.org/10.1016/j.tecto.2016.10.031

Gilbert, G. K. (1877). *Report on the geology of the Henry Mountains: Geographical and geological survey of the Rocky Mountain region*. Washington, DC: U.S. Government Printing Office.

Godt, J. W., Baum, R. L., Savage, W. Z., Salciarini, D., Schulz, W. H., & Harp, E. L. (2008). Transient deterministic shallow landslide modeling: Requirements for susceptibility and hazard assessments in a GIS framework. *Engineering Geology*, *102*(3–4), 214–226. https://doi.org/10.1016/j.enggeo.2008.03.019

Gordon, G. (2014). *Stratigraphic evolution and architectural analysis of structurally confined submarine fans: A tripartite outcrop-based study* (Doctoral dissertation). Golden, CO: Colorado School of Mines. Retrieved from Mountain Scholar (https://mountainscholar.org/handle/11124/278)

Grieve, S. W. D., Mudd, S. M., & Hurst, M. D. (2016). How long is a hillslope? *Earth Surface Processes and Landforms*, *41*(8), 1039–1054. https://doi.org/10.1002/esp.3884

Hack, J. T. (1975). Dynamic equilibrium and landscape evolution. In W. N. Melhorn & R. C. Flemal (Eds.), *Theories of landscape evolution* (pp. 87–102). Boston, MA.

Harp, E. L., & Jibson, R. W. (1995). Inventory of landslides triggered by the 1994 Northridge, California earthquake. In *U. S. Geological Survey Open-File Report 95-213* (pp. 1–18). Reston, VA.

Harp, E. L., & Jibson, R. W. (1996). Landslides triggered by the 1994 Northridge, California, earthquake. *Bulletin of the Seismological Society of America*, *86*(1B), 319–332. https://doi.org/10.3133/ofr95213

Hoek, E., & Brown, E. (1980). Empirical strength criterion for rock masses. *Journal of the Geotechnical Engineering Division*, *106*. https://doi.org/10.1016/0148-9062(81)90766-X

Hoek, E., & Brown, E. (1997). Practical estimates of rock mass strength. *International Journal of Rock Mechanics and Mining Sciences*, *34*(8), 1165–1186. https://doi.org/10.1016/S1365-1609(97)80069-X

Hornafius, J. S., Luyendyk, B. P., Terres, R. R., & Kamerling, M. J. (1986). Timing and extent of Neogene tectonic rotation in the western Transverse Ranges, California (USA). *Geological Society of America Bulletin*, *97*(12), 1476–1487. https://doi.org/10.1130/0016-7606(1986)97<1476:TAEONT>2.0.CO;2

Hovius, N., Stark, C. P., Tutton, M. A., & Abbott, L. D. (1998). Landslide-driven drainage network evolution in a pre-steady-state mountain belt: Finisterre Mountains, Papua New Guinea. *Geology*, *26*(12), 1071–1074. https://doi.org/10.1130/0091-7613(1998)026<1071:LDDNEI>2.3.CO;2

Huftile, G. J., & Yeats, R. S. (1996). Deformation rates across the Placerita (Northridge Mw = 6.7 aftershock zone) and Hopper Canyon segments of the western transverse ranges deformation belt. *Bulletin of the Seismological Society of America*, *86*(1B), 3–18.

Jibson, R. W. (1993). Predicting earthquake-induced landslide displacements using Newmark's sliding block analysis. *Transportation Research Record*, *1411*, 9–17.

Jibson, R. W. (2007). Regression models for estimating coseismic landslide displacement. *Engineering Geology*, *91*(2–4), 209–218. https://doi.org/10.1016/j.enggeo.2007.01.013

Jibson, R. W., Harp, E. L., & Michael, J. A. (2000). A method for producing digital probabilistic seismic landslide hazard maps. *Engineering Geology*, *58*(3–4), 271–289. https://doi.org/10.1016/S0013-7952(00)00039-9

Keefer, D. K. (1994). Landslides caused by earthquakes. *Bulletin of the Seismological Society of America*, *95*, 406–421. https://doi.org/10.1130/0016-7606(1984)95<406:lcbe>2.0.co;2

Korup, O. (2004). Geomorphic implications of fault zone weakening: Slope instability along the alpine fault, South Westland to Fiordland. *New Zealand Journal of Geology and Geophysics*, *47*, 257–267. https://doi.org/10.1080/00288306.2004.9515052

Korup, O. (2008). Rock type leaves topographic signature in landslide-dominated mountain ranges. *Geophysical Research Letters*, *35*, L11402. https://doi.org/10.1029/2008GL034157

Larsen, I. J., Montgomery, D. R., & Korup, O. (2010). Landslide erosion controlled by hillslope material. *Nature Geoscience*, *3*(4), 247–251. https://doi.org/10.1038/ngeo776

Levi, S., & Yeats, R. S. (1993). Paleomagnetic constraints on the initiation of uplift on the Santa Susana Fault, Western Transverse Ranges, California. *Tectonics*, *12*(3), 688–702. https://doi.org/10.1029/93tc00133

Ling, H. I., Mohri, Y., & Kawabata, T. (1999). Seismic analysis of sliding wedge: Extended Francais Culmann's analysis. *Soil Dynamics and Earthquake Engineering*, *18*, 387–393. https://doi.org/10.1016/s0267-7261(99)00005-6

Los Angeles Almanac. Monthly Precipitation (2019) Retrieved from http://www.laalmanac.com/weather/we08aa.php

Lu, N., & Godt, J. W. (2013). Failure surface based stability analysis. In *Hillslope hydrology and stability* (1st ed., pp. 313–363). Cambridge, UK: Cambridge University Press.

Marc, O., & Hovius, N. (2015). Amalgamation in landslide maps: Effects and automatic detection. *Natural Hazards and Earth System Sciences*, *15*(4), 723–733. https://doi.org/10.5194/nhess-15-723-2015

Marc, O., Stumpf, A., Malet, J.-P., Gosset, M., Uchida, T., & Chiang, S.-H. (2018). Initial insights from a global database of rainfall-induced landslide inventories: The weak influence of slope and strong influence of total storm rainfall. *Earth Surface Dynamics*, *6*(4), 903–922. https://doi.org/10.5194/esurf-6-903-2018

Molnar, P., Anderson, R. S., & Anderson, S. P. (2007). Tectonics, fracturing of rock, and erosion. *Journal of Geophysical Research*, *112*, F03014. https://doi.org/10.1029/2005JF000433

Montgomery, D. R. (2001). Slope distributions, threshold hillslopes, and steady-state topography. *American Journal of Science*, *301*, 432–454. https://doi.org/10.2475/ajs.301.4-5.432

Montgomery, D. R., & Brandon, M. T. (2002). Topographic controls on erosion rates in tectonically active mountain ranges. *Earth and Planetary Science Letters*, *201*(3–4), 481–489. https://doi.org/10.1016/S0012-821X(02)00725-2

Montgomery, D. R., & Foufoula-Georgiou, E. (1993). Channel network source representation using digital elevation models. *Water Resources Research*, *29*(12), 3925–3934. https://doi.org/10.1029/93WR02463

Namson, J. S., & Davis, T. L. (1988). Structural transect of the western Transverse Ranges, California: Implications for lithospheric kinematics and seismic risk evaluation. *Geology*, *16*, 675–679. https://doi.org/10.1130/0091-7613(1988)016<0675:stotwt>2.3.co;2

Natural Resources Conservation Service, United States Department of Agriculture. Web soil survey. https://websoilsurvey.sc.egov.usda.gov/

Nicholson, C., Sorlien, C. C., Atwater, T., Crowell, J. C., & Luyendyk, B. P. (1994). Microplate capture, rotation of the western Transverse Ranges, and initiation of the San Andreas transform as a low-angle fault system. *Geology*, *22*(6), 491–495. https://doi.org/10.1130/0091-7613(1994)022<0491:MCROTW>2.3.CO;2

Office for Coastal Management. (2016). *2002/2003 IfSAR data for Southern California: Digital elevation model (NAVD88)*. Charleston, SC: NOAA National Centers for Environmental Information. https://inport.nmfs.noaa.gov/inport/item/48381

Parise, M., & Jibson, R. (2000). A seismic landslide susceptibility rating of geologic units based on analysis of characterstics of landslides triggered by the 17 January, 1994 Northridge, California earthquake. *Engineering Geology*, *58*(3–4), 251–270. https://doi.org/10.1016/S0013-7952(00)00038-7

Prothero, D., & Vance, E. (1996). Magnetostratigraphy of the upper middle Eocene Coldwater Sandstone, central Ventura County, California. In D. Protherno, & R. Emry (Eds.), *The terrestrial Eocene-Oligocene transition in North America* (pp. 155–170). Cambridge, U.K.: Cambridge University Press.

Riebe, C. S., Hahm, W. J., & Brantley, S. L. (2017). Controls on deep critical zone architecture: A historical review and four testable hypotheses. *Earth Surface Processes and Landforms*, *42*(1), 128–156. https://doi.org/10.1002/esp.4052

Rockwell, T. (1988). Neotectonics of the San Cayetano fault, Transverse Ranges, California. *Geological Society of America Bulletin*, *100*, 500–513. https://doi.org/10.1130/0016-7606(1988)100<0500:notscf>2.3.co;2

Roering, J. J., Kirchner, J. W., & Dietrich, W. E. (1999). Evidence for nonlinear, diffusive sediment transport on hillslopes and implications for landscape morphology. *Water Resources Research*, *35*(3), 853–870. https://doi.org/10.1029/1998WR900090

Roering, J. J., Perron, J. T., & Kirchner, J. W. (2007). Functional relationships between denudation and hillslope form and relief. *Earth and Planetary Science Letters*, *264*(1–2), 245–258. https://doi.org/10.1016/j.epsl.2007.09.035

Roy, S. G., Koons, P. O., Upton, P., & Tucker, G. E. (2015). The influence of crustal strength fields on the patterns and rates of fluvial incision. *Journal of Geophysical Research: Earth Surface*, *120*, 275–299. https://doi.org/10.1002/2015JF003602

Sarma, S. K. (1981). Seismic displacement analysis of earth dams. *Journal of the Soil Mechanics and Foundations Division*, *107*(2), 1735–1739.

Scheingross, J. S., Minchew, B. M., Mackey, B. H., Simons, M., Lamb, M. P., & Hensley, S. (2013). Fault-zone controls on the spatial distribution of slow-moving landslides. *Geological Society of America Bulletin*, *125*(3/4), 473–489. https://doi.org/10.1130/B30719.1

Schmidt, K. M., & Montgomery, D. R. (1995). Limits to relief. *Science*, *270*(5236), 617–620. https://doi.org/10.1126/science.270.5236.617

Selby, M. J. (1980). A rock mass strength classification for geomorphic purposes: With tests from Antarctica and New Zealand. *Zeitschrift für Geomorphologie*, *24*, 31–51.

Selby, M. J. (1993). *Hillslope materials and processes*. Oxford: Oxford University Press.

Sklar, L. S., & Dietrich, W. E. (2001). Sediment and rock strength controls on river incision into bedrock. *Geology*, *29*(12), 1087–1090. https://doi.org/10.1130/0091-7613(2001)029<1087:SARSCO>2.0.CO

Stock, J., & Dietrich, W. E. (2003). Valley incision by debris flows: Evidence of a topographic signature. *Water Resources Research*, *39*(4), 1089. https://doi.org/10.1029/2001WR001057

Tarboton, D., Bras, R., & Rodriguez-Iturbe, I. (1991). On the extraction of channel networks from digital elevation data. *Hydrological Processes*, *5*(1), 81–100. https://doi.org/10.1002/hyp.3360050107

U.S. Geological Survey. (1994). Advanced National Seismic System (ANSS), ShakeMap, Global Region, Maps of ground shaking and intensity for event 19940117123055, Northridge, California, v1. https://earthquake.usgs.gov/earthquakes/eventpage/ci3144585/shake-map/intensity

U.S. Geological Survey (and California Geological Survey). (2006). Quaternary fault and fold database for the United States, from USGS web site: http//earthquake.usgs.gov/hazards/qfaults

Whipple, K. X., Kirby, E., & Brocklehurst, S. H. (1999). Geomorphic limits to climate-induced increases in topographic relief. *Nature*, *401*, 39–43. https://doi.org/10.1038/43375

Wieczorek, G. F., Wilson, R. C., & Harp, E. L. (1985). *Map showing slope stability during earthquakes in San Mateo County, California* (Map no 1257-E, scale 1:62,500). Reston, VA: U.S. Geological Survey.

Willett, S. D., & Brandon, M. T. (2002). On steady state in mountain belts. *Geology*, *30*(2), 175–178. https://doi.org/10.1130/0091-7613(2002)030<0175

Worden, R. H., & Burley, S. D. (2003). Sandstone diagenesis: The evolution of sand to stone. In *Sandstone Diagenesis: Recent and Ancient* (pp. 3–44). Malden, MA: Blackwell Publishing.

Wright, T. L. (1991). Structural geology and tectonic evolution of the Los Angeles Basin, California. In K. T. Biddle (Ed.), *Active margins basins* (pp. 35–135). Tulsa, OK: American Association of Petroleum Geologists Memoir 52.

Yeats, R. S., Huftile, G. J., & Stitt, L. T. (1994). Late Cenozoic tectonics of the east Ventura basin, Transverse Ranges, California. *American Association of Petroleum Geologists Bulletin*, *78*. https://doi.org/10.1306/A25FE42D-171B-11D7-8645000102C1865D

Yeats, R. S., Mcdougal, J. W., & Stitt, L. T. (1986). *Cenozoic structure of the Val Verde 7 1/2-minute quadrangle and south half of the Whitaker Peak 7 1/2-minute quadrangle California* (United States Geological Survey Open File Report 85-587, p. 24). Reston, VA